Plasma Sources Science and Technology



**PAPER** • **OPEN ACCESS**

# Modeling the hundreds-of-nanoseconds-long irradiation of tin droplets with a 2 $\mu$m-wavelength laser for future EUV lithography

To cite this article: S J J de Lange *et al* 2024 *Plasma Sources Sci. Technol.* **33** 105003



OPEN ACCESS
IOP Publishing
Plasma Sources Science and Technology
Plasma Sources Sci. Technol. **33** (2024) 105003 (13pp)
https://doi.org/10.1088/1361-6595/ad7c7c

# Modeling the hundreds-of-nanoseconds-long irradiation of tin droplets with a 2 $\mu$m-wavelength laser for future EUV lithography

**S J J de Lange[1,2], D J Hemminga[1,2], Y Mostafa[1,2], R A Meijer[1], O O Versolato[1,2] and J Sheil[1,2,*]**

[1] Advanced Research Center for Nanolithography, Science Park 106, 1098 XG Amsterdam, The Netherlands
[2] Department of Physics and Astronomy, and LaserLaB, Vrije Universiteit Amsterdam, De Boelelaan 1081, 1081 HV Amsterdam, The Netherlands

E-mail: j.sheil@arcnl.nl

Received 6 May 2024, revised 30 August 2024
Accepted for publication 18 September 2024
Published 7 October 2024

**Abstract**

The properties of an extreme ultraviolet (EUV) source driven by hundreds-of-nanoseconds-long laser pulses of $\lambda_{\text{laser}} = 2$ $\mu$m wavelength are investigated through radiation-hydrodynamic simulations. We show that single-pulse irradiation of 30 $\mu$m-diameter tin droplets can generate in-band energies $\sim$30 mJ directed in the $2\pi$ sr solid angle subtended by the collector mirror, yielding energies $\sim$100 mJ produced from 45 $\mu$m-diameter droplets. Time-integrated in-band EUV emission profiles, generated by taking Abel transforms of the local net in-band emissivity, reveal EUV source sizes in the axial (laser) direction $\times$ radial direction of $\sim$600 (1000) $\times$ 100 (150) $\mu$m$^2$ for 30 (45) $\mu$m-diameter droplets. We find that approximately 74% of the total in-band emission is produced during the first half of the total propulsion distance irrespective of droplet size or laser intensity. Furthermore, we propose a one-dimensional analytical propulsion model to qualitatively explain the simulated droplet trajectory and to predict the time taken for the droplet to vaporize. These findings offer motivation for the development of high-power EUV sources based on single-pulse, hundreds-of-nanoseconds-long irradiation of tin droplets.

Keywords: EUV, nanolithography, lasers, plasma sources, etendue, plasma modeling

## 1. Introduction

Laser-produced plasmas (LPPs) are a compact, versatile means of generating intense, tunable, short-wavelength radiation [1, 2]. In addition to facilitating fundamental investigations of atomic structures and plasma properties [3, 4], LPP radiation is utilized in applications spanning biological imaging [5, 6], inertial confinement fusion [7], and the printing of nanometer-scale patterns on silicon wafers in new-generation semiconductor manufacturing [8–10]. This latter application, known as extreme ultraviolet lithography (EUVL), serves as the main motivation for the present work.

The light source incorporated in EUVL machines is that of a hot (electron temperature $T_e \sim$ 30–50 eV) and dense (electron density $n_e \sim 10^{19}$ cm$^{-3}$) laser-produced tin plasma [11–13].

* Author to whom any correspondence should be addressed.

Under optimum conditions, this plasma produces an intense, narrowband emission feature peaked near a wavelength of 13.5 nm [14–17]. Crucially, this emission feature overlaps with the wavelengths reflected by Mo/Si multilayer mirrors [18] (13.5 ± 0.135 nm—the 'in-band' region), mirrors whose purpose is to filter, transport, and shape the in-band radiation for the lithographic process. The first of these mirrors is called the collector mirror. Located in the source vessel, it serves to focus the EUV from the source, and subtends a $2\pi$ sr solid angle around the plasma. High-power $CO_2$ lasers ($\lambda_{laser} = 10.6\,\mu$m) create these plasmas from tin targets that are 'conditioned' by a pre-pulse laser [19, 20]. This process ensures maximal absorption of $CO_2$ laser light, which, in turn, underlies the high in-band EUV powers ($P_{inband}$) and conversion efficiencies [20] (CE—the ratio of in-band energy radiated in the $2\pi$ sr hemisphere in the direction of the collector mirror to laser energy [21]) attained in industrial EUV sources. Industrial sources currently operate at $P_{inband} \sim 250$ W, and efforts to scale this power to $P_{inband} \sim 600$ W (demonstrated in a research setting in [22]) are ongoing to drive increased wafer throughput.

While $CO_2$ lasers form the basis of current EUV source design, the research community is now questioning whether a more modern, energy-efficient laser architecture, such as solid-state $\lambda_{laser} \sim 2\,\mu$m Tm:YLF lasers [23, 24], could drive EUV sources of the future. In addition to demonstrating high CE values in EUV source simulations [25], these systems promise excellent pulse shaping capabilities, scalability to high laser powers and repetition rates, as well as high efficiencies in converting electrical power to laser light (up to ∼20% [26])—an attractive feature in the drive for a greener semiconductor industry. Laser development has advanced rapidly in recent times, with Tamer *et al* reporting the development of a 1 GW peak power, 100 J Tm:YLF-based 2 $\mu$m system [27]. The goal of the current paper is to investigate, using analytical and numerical means, the properties of EUV source plasmas driven by such advanced laser systems.

Here follows a brief overview of 2 $\mu$m-driven EUV source research to date. First experiments on 2 $\mu$m-driven tin plasmas, utilizing a master-oscillator power amplifier system, reported conversion efficiencies CE ∼3% for irradiation of tin slab targets [28]—nearly a factor two higher than the Nd:YAG ($\lambda_{laser} = 1.064\,\mu$m) case, under similar conditions. This was soon followed by a characterization of EUV spectra from spherical [29] and disk-shaped [30] targets. Efforts to increase CE further were made by Mostafa *et al* [31] who reported CE ∼5% using quasi-flat-top spatial and temporal laser profiles [32]. As discussed in that study, it is the flat-top nature of these laser profiles that provides uniform heating of the plasma that drives this CE increase. On the theoretical front, radiation-hydrodynamic modeling has enabled the characterization of laser-to-plasma power partitioning [33], provided an understanding of high CE performance [33–35], and has led to the proposal of novel irradiation schemes to drive CE increases [36]. The primary challenge now facing the research community is to identify a 2 $\mu$m-driven plasma recipe that can generate EUV powers exceeding those of current industrial systems. The current study will investigate one specific embodiment of such a recipe: irradiating tin droplets with a single, high-energy 2 $\mu$m laser pulse until complete droplet vaporization.

In this work, we present the results of laser–plasma simulations of hundreds-of-nanoseconds-long 2 $\mu$m-wavelength irradiation of tin droplets. We show that this scheme can generate single-shot in-band energies $E_{inband} \sim 30$ mJ directed towards the collector mirror from irradiation of 30 $\mu$m-diameter-droplets. We show that even higher in-band energies $E_{inband} \sim 100$ mJ can be produced from 45 $\mu$m-diameter droplet irradiation. A strong stability of instantaneous CE is identified over the course of laser irradiation, as well as a small reduction in CE for laser intensities above the CE-generating optimum. This latter aspect is exploited to generate high in-band energies by using laser intensities above the optimum for CE. The EUV source sizes are quantified by taking Abel transforms of the local net in-band emissivity, revealing extensions in the axial (laser) direction × radial direction of ∼600 (1000) × 100 (150) $\mu$m$^2$ for 30 (45) $\mu$m diameter droplets. We find that approximately 74% of the total in-band emission is produced during the first half of the total propulsion distance irrespective of droplet size or laser intensity. A one-dimensional analytical propulsion model has been developed, which, upon inclusion of a droplet size-independent scaling factor, reproduces the time taken to vaporize the droplet as predicted by the simulations.

The structure of the paper is as follows: in section 2, we provide details of the radiation-hydrodynamic simulations performed in this work. This is followed in section 3 by an extensive characterization of EUV source properties: source size, droplet trajectory dynamics, the dependence of $E_{inband}$ and CE on droplet size and laser intensity, as well as a brief study on the impact of laser refraction on EUV source properties. Finally, the work is concluded in section 4.

## 2. Radiation-hydrodynamic simulations

Radiation-hydrodynamic simulations of a single-pulse-on-droplet irradiation scheme were performed using the two-dimensional Radiative Arbitrary Lagrangian–Eulerian Fluid dynamics (RALEF-2D) code [37]. Its strength lies in modeling high-temperature, strongly radiating laser-plasmas, finding application in radiation-driven implosion studies [38], ion-stopping in warm dense matter [39, 40] and EUV source plasma research [29, 41–43]. A detailed description of the physical models and numerical methods implemented in the code can be found in [42, 44], and only a brief overview follows.

### 2.1. Code details

RALEF-2D solves the equations of single-fluid, single-temperature hydrodynamics including the processes of

thermal conduction, radiation transport, and energy deposition through 'external' sources, such as laser heating. The hydrodynamic component of RALEF-2D is based on an upgraded version of the CAVEAT code [45], with thermal conduction and radiation transport modules implemented via the symmetric semi-implicit method [46, 47]. The equation of quasi-static, local thermodynamic equilibrium (LTE) radiation transfer, written

$$\hat{\Omega} \cdot \nabla I_\lambda = \alpha_\lambda \left( B_\lambda - I_\lambda \right), \tag{1}$$

is solved using the method of short characteristics [48]. Here $\hat{\Omega}$ is a unit vector representing the photon propagation direction, $I_\lambda$ is the wavelength ($\lambda$)-dependent specific intensity, $\alpha_\lambda$ is the absorption coefficient and $B_\lambda$ is Planck's law for blackbody spectral radiance. Absorption coefficients are derived from steady-state non-LTE calculations performed with the THERMOS code [41, 49, 50]. As per the nomenclature of [51], we will refer to the right-hand-side of equation (1) as the net emissivity $\varepsilon_\lambda$. The angular dependence of $I_\lambda$ was modeled using the $S_n$ method [52] with $n = 6$.

Laser light propagation is treated using a hybrid model that couples a geometrical-optics ray-tracing approach in underdense plasma regions with a wave optics treatment in regions near and beyond the critical electron density [47]. To avoid stochastic effects, the simulations performed (except for the control runs in section 3.3) did not simulate laser refraction in the plasma: light can only be absorbed or reflected. A brief study on the effects of laser refraction on CE is also presented in section 3.3. As in our previous work [33], the laser absorption coefficient is derived from the complex dielectric permittivity of the plasma according to the Drude model [53]. Equation-of-state (EOS) parameters, such as pressure and average charge state, were obtained from the FEOS model [54, 55].

### 2.2. Target and laser conditions

In the following, we perform two-dimensional axially symmetric simulations of 2 $\mu$m irradiation of tin droplets with initial diameters $D =$ 30, 40, and 45 $\mu$m. The structure of the computational mesh is similar to our previous work [56] we progressively refine the mesh thickness to a value of ∼30 nm at the droplet surface. The adaptive Lagrangian–Eulerian mesh maintains a thickness of ∼500 nm at the critical electron density surface (similar to that found in [57]). To ensure homogeneous heating of the plasma over the course of laser irradiation, box-shaped temporal and spatial laser profiles are employed. The temporal duration is chosen to ensure complete vaporization of the droplet target, and the spatial width (following [33]) is taken to be twice that of the initial droplet diameter over the full course of laser irradiation. As evidenced from figure 1(b) of [33], this spatial profile ensures high laser absorptivity due to its significant overlap with the critical electron density surface, i.e. only a very small fraction of incident laser light passes around the target. These choices are further motivated by the recent experiments of Mostafa *et al* [31] who demonstrated high CE performance arising from box-shaped laser illumination of tin sheets.

What differentiates the current work from previous theoretical studies on the subject [33–36] is the present goal of producing industrial-grade, in-band EUV energies (tens of mJ) from a 2 $\mu$m-driven plasma. Maximizing in-band production from a main pulse-only scheme requires converting as much of the initial liquid target into in-band emitting ions as possible, which requires full vaporization of the target. Inspired by the findings of Hemminga *et al* [33] we investigate the feasibility of using laser intensities above the CE-maximal value ($I_{\text{laser}} \sim 0.7 \times 10^{11}$ W cm$^{-2}$ for 2 $\mu$m-driven plasmas [21]) to generate high $E_{\text{inband}}$ values with minimal impact on CE.

## 3. Analysis of simulations and theoretical modeling

In the following, we characterize the properties of the EUV source: source size, in-band energy $E_{\text{inband}}$ production as a function of propulsion distance, instantaneous CE, and mass ablation rate. We also provide a brief study on the impact of laser refraction (in the plasma) on EUV source properties.

### 3.1. Time-integrated in-band profiles

A key parameter in lithography is the étendue of the EUV source. Defined as the area of the EUV-emitting plasma times the solid angle subtended by the collector optics, it characterizes the ability of the collector mirror to focus in-band radiation, and is therefore an important aspect of EUV source design. Its exact value depends on the system's optical specifics, as noted by Fomenkov *et al* [20].

In figure 1 we present images of the droplet morphology for laser illumination of tin droplets having diameters (a) $D =$ 30 $\mu$m and (c) $D = 45\,\mu$m. A laser intensity $I_{\text{laser}} = 1.4 \times 10^{11}$ W cm$^{-2}$ is employed in both cases, and the droplet images correspond to times $t = 0, 75, 100, 125, \ldots$ ns after the pulse is switched on. By conservation of momentum, the droplet is propelled in the $+\hat{z}$-direction as ablated material is ejected primarily in the collector-mirror-directed half-space [58]. The droplet undergoes significant morphological changes throughout laser irradiation. A quantitative study of the droplet trajectory follows in appendix A.2 below, and we leave the investigation of late-time droplet morphology to future work.

Despite the droplet deformation, the radial size of the EUV source is remarkably constant over time. In figures 1(b) and (d) we present time-integrated in-band images for the $D = 30$ and 45 $\mu$m droplet diameters, respectively. This is done by taking Abel transforms [59] of positive values of the local net in-band emissivity $\epsilon_{\text{inband}}$ at each time, and then summing them up. The quantity shown is therefore an in-band *fluence* (units: mJ $\mu$m$^{-2}$) [33]. This transform maps the 2D axially-symmetric in-band emission onto a 2D plane as would be visualized in experiments. It is seen that the radial extent of the source size does not shrink substantially over the course of laser irradiation. The accumulation of high $\epsilon_{\text{inband}}$ values

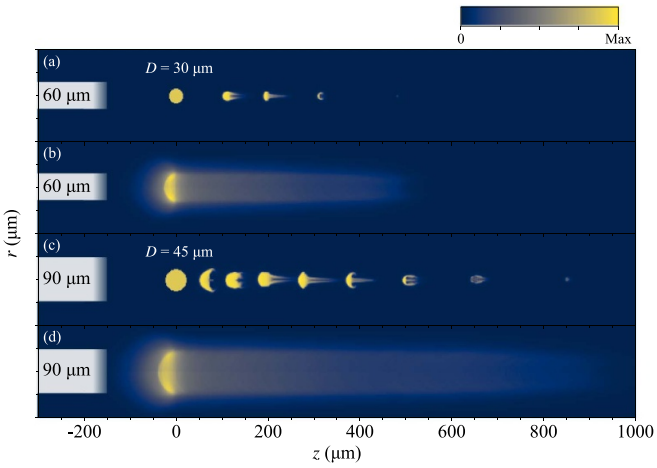


**Figure 1.** (a) Simulated density profile of a $D = 30\,\mu$m-diameter droplet irradiated by a 2 $\mu$m-wavelength laser pulse of intensity $I_{\text{laser}} = 1.4 \times 10^{11}$ W cm$^{-2}$ at times $t = 0, 75, 100, 125\ldots$ ns after the pulse is switched on. The pulse is incident from $z = -\infty$, and its spatial extent is indicated by the gray-shaded region. (b) Time-integrated in-band image obtained by Abel-transforming positive values of the local net in-band emissivity $\epsilon_{\text{inband}}$. Sub-panels (c) and (d) are the same as (a) and (b) but for a 45 $\mu$m diameter droplet, and are plotted on a common intensity scale, with $\rho_{\text{max}} = 7.7$ g cm$^{-3}$, and a maximum in-band fluence of $3.2 \times 10^{-3}$ mJ $\mu$m$^{-2}$.

close to the initial position of the droplet ($z = r = 0\,\mu$m), visible as the bright yellow region, is due to the droplet's inertia: the droplet remains near the origin for a relatively long time, radiating EUV continuously. This bright 'core' of EUV is then followed by a vanishing 'tail' to the right as the target accelerates and decreases in mass. We also observe that very little in-band radiation is produced at distances $z > 600\,(1000)\,\mu$m for the $D = 30$ (45) $\mu$m cases: these positions coincide with the position at which the droplet is fully vaporized, i.e. the position where the maximum density in the target falls below a density of $\rho_{\text{vap}} = 1.0$ g cm$^{-3}$. We will refer to the time at which this occurs as the 'vaporization time' $t_{\text{vap}}$, and the corresponding position as the 'vaporization position' $z_{\text{vap}}$.

These images give a first impression of an EUV source size that could be expected from such an irradiation scheme. The radial extent of the $D = 30\,\mu$m case, $r \sim 100\,\mu$m, is approximately four times smaller than that observed in the experiments of Tomita *et al* (see figure 1(g) of [11]), who employ a pre-pulse–$CO_2$ main pulse irradiation scheme starting with a 26 $\mu$m-diameter droplet. The $z$-extent of in-band emission in the 2 $\mu$m-driven scheme is on the order of 600 (900) $\mu$m for the $D = 30\,(45)\,\mu$m cases. Tomita *et al* [11] report a $z$-extent of $\sim$400 $\mu$m, comparable to a value of 600 $\mu$m value recorded from direct irradiation of 30 $\mu$m-diameter droplets. We thus see that our single-pulse irradiation scheme has a smaller EUV emitting area than the multi-pulse industrial scheme characterized in [11].

The current approach of Abel-transforming $\epsilon_{\text{inband}}$ neglects the effects of radiation transport and thus assumes an optically thin medium. To study the importance of self-absorption, we plot in figure 2 the optical thickness $\tau$ (blue curves) along the $z$ (laser) axis at times $t = 75, 100$ and 125 ns. This quantity is defined as the line integral of the absorption coefficient $\alpha$ (green) along the $-z$-axis: $\tau(z) = \int_z^{-\infty} \alpha(z')\mathrm{d}z'$. In general, large $\tau(z)$ means that most in-band radiation emitted at $z$ is reabsorbed in the medium, and the plasma is opaque at this depth. You see from figure 2 that the optical depth rises sharply just behind the critical surface: this is because of the sharp rise in $\alpha$ due to the presence of EUV-absorbing charge states $Z \in [11^+, 15^+]$. A lineout of $T_e$ is shown in light blue, and the orange dash-dotted curve represents the average charge state $Z_{\text{ion}}$; this is a useful heuristic for understanding the emission and absorptive properties of the plasma. In the Thomas–Fermi model [41, 60], $Z_{\text{ion}}$ is related to the electron temperature $T_e$ by a power law $Z_{\text{ion}} = 1.4T_e^{0.6}$. The maximum $T_e$ at $t = 100$ ns, for example, is $T_e = 71$ eV, giving a maximum average charge state $Z_{\text{ion}} \sim 19$: this is above the optimal charge state range for in-band production. (For the $I_{\text{laser}} = 0.7 \times 10^{11}$ W cm$^{-2}$ case, the maximum values are $T_e = 49$ eV and $Z_{\text{ion}} = 15$.)

We also present in figure 2 the net in-band emissivity $\epsilon_{\text{inband}}$ profile (red curve). A few $\mu$m behind the critical surface, this quantity peaks. This is due to a coincidental decrease of $Z_{\text{ion}}$ to optimal values: here the plasma contains large populations of in-band-emitting charge states, and thus a relatively large fraction of in-band radiation is produced. As one moves closer to the droplet surface, absorption dominates ($\epsilon_{\text{inband}} < 0$), and $\tau$ rises steeply. If the radiation field is sufficiently intense, this can lead to the formation of a 'radiation-soaked' ablation front [41], known also as a multiablation structure [61]. We note the local $\epsilon_{\text{inband}}$ minimum at $z = 168\,\mu$m. This is due to local overheating by the laser, leading to super-optimal $Z_{\text{ion}}$ and low in-band EUV emission [33]. For the $I_{\text{laser}} = 0.7 \times 10^{11}$ W cm$^{-2}$ case at $t = 50$ ns (not shown), we find that $\epsilon_{\text{inband}}$ peaks just in front of the critical surface and is more 'extended' in the $-z$ direction compared to the higher-intensity case. This is because the optimal EUV-emitting charge states are bred in a comparatively wider zone. The optical depth at the critical surface in this case is $\tau \sim 0.8$, substantially higher than the higher-intensity case. Lastly, the invariance of the quantities in figure 2 demonstrates the steady-state nature of the system. A similar figure for the $D = 45\,\mu$m-diameter droplet case is presented in figure 7 in the appendix.

At this point it is worth commenting on the optical depth values presented in figure 2. In the intense EUV-emitting region behind the critical surface, $\tau \sim 0.4$: a rather small value. Use of an Abel transform at late times may therefore be appropriate. However, we should note that the experiments of Schupp *et al* [29] have, through spectroscopic means, reported a higher value of $\tau \sim 2$. We have a few hypotheses for this difference. Values of $\tau$ inferred from experimental spectra were time integrated over short-pulse irradiation ($\sim$5 ns) of droplets with $D > 20$ $\mu$m. Moreover, the spectra were recorded at an

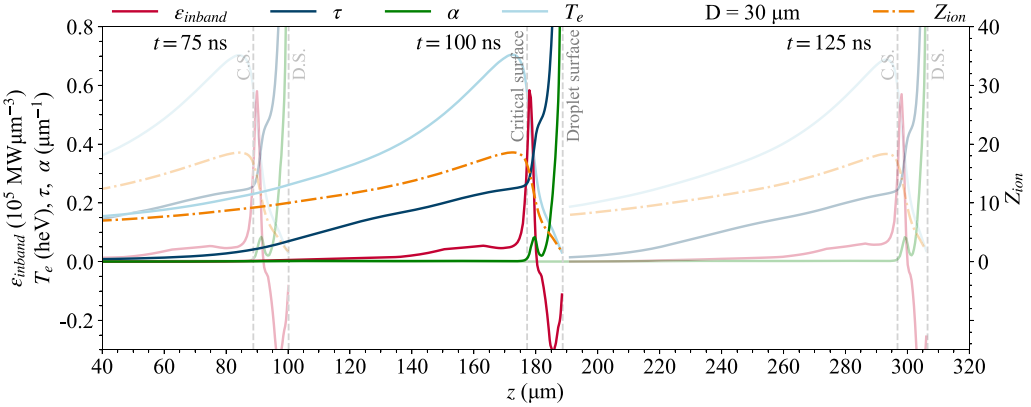


**Figure 2.** One-dimensional profiles taken along the laser axis for $I = 1.4 \times 10^{11}$ W cm$^{-2}$ irradiation of a $D = 30\,\mu$m tin droplet taken at 75, 100, and 125 ns. $\epsilon_{\text{inband}}$ is the net in-band power per unit of volume, shown in red. The optical thickness $\tau(z)$ (blue), is defined as $\int_z^{-\infty} \alpha(z')\mathrm{d}z'$ and $\alpha$ is the absorption coefficient (green). $T_e$ is the electron temperature (light blue), and $Z_{\text{ion}}$ is the average charge state (orange dash-dotted curve).

angle of 60° with respect to the laser axis. Values for $\tau$ calculated in the present work are (i) instantaneous, (ii) recorded at late times when the plasma size is (most probably) smaller than in the experiments and (iii) taken along the $z$-axis. In essence, the integral defining the optical depth, $\int_z^{-\infty} \alpha(z')\mathrm{d}z'$, is different for experiments and simulation, hence the differences in $\tau$.

As noted above, figure 1 reveals that the spatial in-band emission is characterized by a core and a tail. In light of the aforementioned discussion on the étendue of the source, we present in figure 3 a quantitative picture of in-band production as a function of center-of-mass position $z$ for laser intensities $I_{\text{laser}} = 0.7, 1.4, 2.1, 2.8$ and $3.5 \times 10^{11}$ W cm$^{-2}$ (ordered from light to dark blue). The curves reveal how much useful in-band energy $E_{\text{inband}}$ is directed into the $2\pi$ sr solid angle subtended by the collector mirror within a certain distance from the droplet origin. The curves end where the maximum density in the target falls below $\rho_{\text{vap}}$. The precise value chosen for $\rho_{\text{vap}}$ is of little consequence to the results: near vaporization, the maximum density drops rapidly, and doubling or halving the definition of $\rho_{\text{vap}}$ would incur an error of a few ns at most; furthermore, as can be seen from figure 4(a) below, EUV production ceases shortly after $t_{\text{vap}}$.

Two important observations from figure 3 are (i) the increase in total $E_{\text{inband}}$ yield, i.e. the value at $t_{\text{vap}}$, with increasing laser intensity, and (ii) the clear plateauing of $E_{\text{inband}}$ for high laser intensities. Both trends will be further substantiated in the next subsection, where we quantify the instantaneous CE for all cases. Curiously, when center-of-mass position is plotted against $E_{\text{inband}}$ relative to their values at $t_{\text{vap}}$, shown in the inset of figure 3, significant overlap of the curves exists, though there is variation in $z_{\text{vap}}$. Moreover, from the inset one sees that approximately 74% of the total in-band radiation for all laser intensities is generated in the first half of the total propulsion distance. This also extends to the 45 $\mu$m-diameter case–see figure 8 in the appendix. This finding is important to consider when quantifying the source size and its coupling to the étendue of the system.

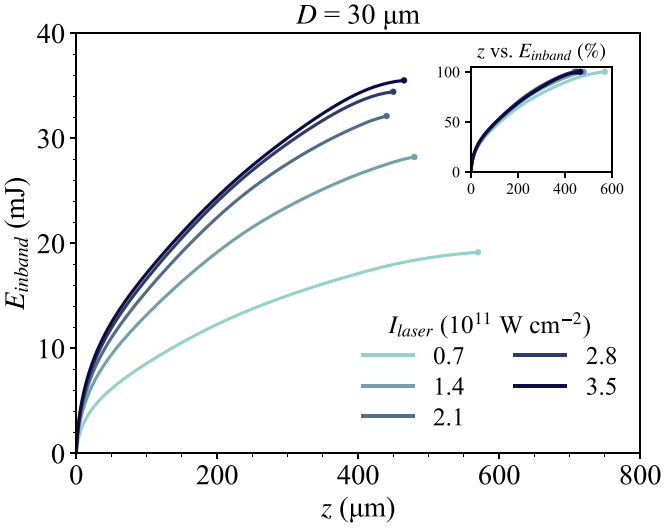


**Figure 3.** Cumulative in-band radiation $E_{\text{inband}}$ directed into the $2\pi$ sr solid angle subtended by the collector mirror as a function of droplet center-of-mass position $z$ for $D = 30\,\mu$m-diameter droplet irradiation. The curves correspond to laser intensities $I_{\text{laser}} = 0.7, 1.4, 2.1, 2.8$, and $3.5 \times 10^{11}$ W cm$^{-2}$ (ordered from light to dark blue). The inset shows the same curves plotted relative to their respective final $E_{\text{inband}}$ values.

### *3.2. Instantaneous conversion efficiency, droplet trajectory dynamics, and mass ablation rate*

From the above analysis, three questions arise: How does CE change over time? How does CE depend on laser intensity? How do the droplet trajectory and mass ablation rate depend on time and laser intensity?

Addressing the first two questions, we plot in figure 4(a) the instantaneous CE obtained by irradiating a 30 $\mu$m-diameter droplet with laser intensities $I_{\text{laser}} = 0.7, 1.4, 2.1, 2.8$, and $3.5 \times 10^{11}$ W cm$^{-2}$ (ordered from light to dark blue). The dashed gray vertical lines indicate the vaporization time $t_{\text{vap}}$. Values of $E_{\text{laser}}$ (laser energy emitted up until $t_{\text{vap}}$),

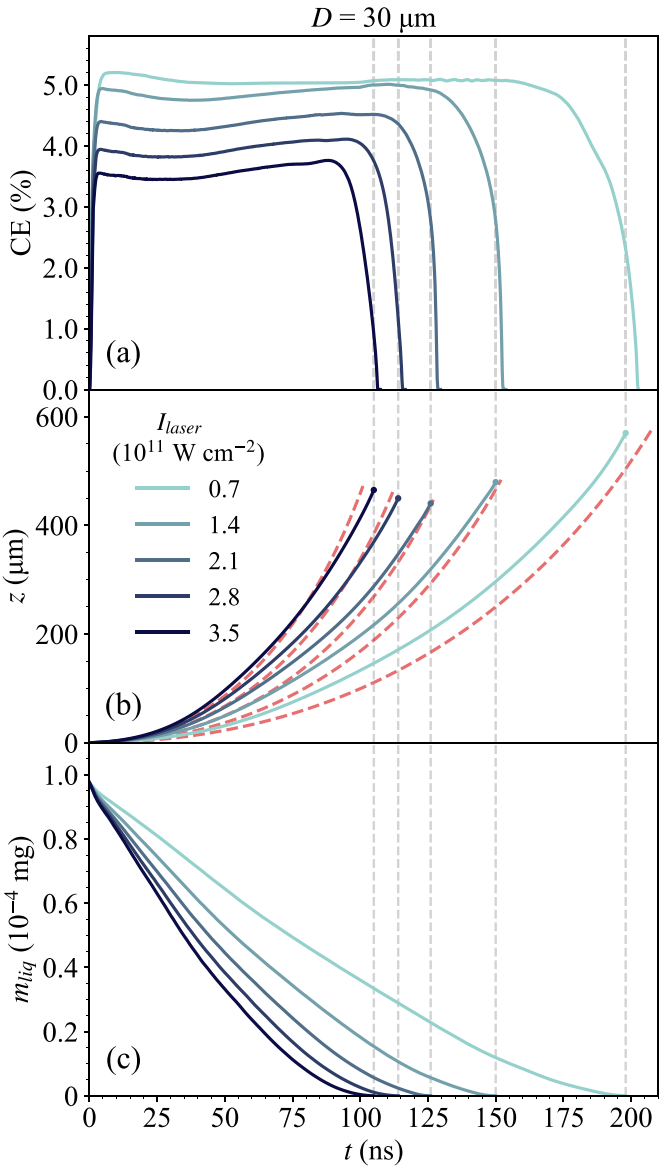


**Figure 4.** (a) Instantaneous conversion efficiency (CE) for $I_{\text{laser}} = 0.7, 1.4, 2.1, 2.8$, and $3.5 \times 10^{11}$ W cm$^{-2}$ irradiation (ordered from light to dark blue) of $D = 30\,\mu$m-diameter droplets. The vaporization time $t_{\text{vap}}$ for each case is indicated by the dashed gray vertical line. (b) The center-of-mass position $z$ of the droplet over time. The dashed red curves are the trajectories of the droplet predicted by the theory proposed in this paper. Simulated values for $z_{\text{vap}}$ were used as input. (c) The amount of liquid mass (material having density $\rho > 1$ g cm$^{-3}$) remaining in the target as a function of time.

$t_{\text{vap}}$, time-integrated conversion efficiency $\text{CE}_{\text{int}}$, and in-band energy $E_{\text{inband}}$ emitted in the direction of the collector mirror are provided in table 1 alongside the corresponding laser intensity $I_{\text{laser}}$.

For the lowest, CE-maximizing intensity ($I_{\text{laser}} = 0.7 \times 10^{11}$ W cm$^{-2}$), it takes approximately 10 ns for the plasma to reach a steady-state flow regime, wherein the different energy channels are approximately constant [33]. While the droplet is losing mass, a near-constant instantaneous CE of 5.0% is maintained up until $t = 155$ ns; at this time, the critical surface has retracted to the point that laser light in the periphery of the beam is no longer absorbed. The near-constancy in CE observed in figure 4(a) is perhaps surprising given the significant morphological changes of the droplet over the course of vaporization, cf figure 1(a). At $t \approx 175$ ns, the droplet contains only 10% of its initial mass and CE begins decreasing rapidly. At $t = 198$ ns, a total of 19.1 mJ of in-band radiation has been emitted in the direction of the collector mirror, with an integrated conversion efficiency of $\text{CE}_{\text{int}} \sim 4.9\%$. This is in good agreement with the value $\text{CE}_{\text{int}} \sim 4.5\%$ measured in the experiments of Mostafa *et al* [31].

**Table 1.** Laser parameters and EUV source properties for laser irradiation of 30, 40 and 45 $\mu$m-diameter droplets. $E_{\text{laser}}$ is the laser energy used up until the vaporization time $t_{\text{vap}}$. $\text{CE}_{\text{int}}$ is the integrated CE at $t = t_{\text{vap}}$. $E_{\text{inband}}$ is the total amount of in-band energy directed into the $2\pi$ sr solid angle subtended by the collector mirror.

| $I_{\text{laser}}$ ($10^{11}$ W cm$^{-2}$) | $E_{\text{laser}}$ (J) | $t_{\text{vap}}$ (ns) | $\text{CE}_{\text{int}}$ (%) | $E_{\text{inband}}$ (mJ) |
|---|---|---|---|---|
| | | $D = 30\ \mu$m | | |
| 0.7 | 0.4 | 198 | 4.9 | 19.1 |
| 1.4 | 0.6 | 150 | 4.7 | 28.3 |
| 2.1 | 0.8 | 126 | 4.3 | 32.2 |
| 2.8 | 0.9 | 114 | 3.8 | 34.5 |
| 3.5 | 1.0 | 105 | 3.4 | 35.5 |
| | | $D = 40\ \mu$m | | |
| 0.7 | 1.1 | 303 | 4.6 | 49.5 |
| 1.4 | 1.5 | 216 | 4.4 | 69.9 |
| 2.1 | 2.0 | 185 | 4.0 | 79.4 |
| 2.8 | 2.4 | 167 | 3.5 | 84.3 |
| 3.5 | 2.7 | 154 | 3.1 | 86.3 |
| | | $D = 45\ \mu$m | | |
| 0.7 | 1.6 | 348 | 4.6 | 72.1 |
| 1.4 | 2.3 | 255 | 4.6 | 101.2 |
| 2.1 | 2.8 | 210 | 4.1 | 112.0 |
| 2.8 | 3.4 | 190 | 3.6 | 118.9 |
| 3.5 | 3.8 | 169 | 3.2 | 118.7 |

In table 1, we provide values for the integrated CE at $t = t_{\text{vap}}$, $\text{CE}_{\text{int}}$, and the cumulative in-band energy $E_{\text{inband}}$. In line with the findings of Hemminga *et al* [33] we see that increasing the laser intensity above the CE-maximizing value leads to a substantial gain in $E_{\text{inband}}$ and only a minor reduction in $\text{CE}_{\text{int}}$. Doubling the intensity to $I_{\text{laser}} = 1.4 \times 10^{11}$ W cm$^{-2}$, for instance, increases $E_{\text{inband}}$ by 48% while $\text{CE}_{\text{int}}$ diminishes by just 0.13%. The difference in in-band production between the two lowest intensity cases (0.7 and $1.4 \times 10^{11}$ W cm$^{-2}$) can be understood as the result of a trade-off between laser intensity, $t_{\text{vap}}$, and (to a lesser extent) CE: higher intensities deposit more energy onto the target, but this process occurs for a shorter time (mass ablation rate increases with increasing laser intensity) and causes the CE to depreciate (as the target is heated above CE-optimal temperatures). Increasing the laser intensity further leads to marginal increases in $E_{\text{inband}}$ (see figure 3). That said, the instantaneous CE in all laser intensity cases is remarkably stable for most of the vaporization process. Also provided in table 1 are results from laser irradiation of 40 and

45 $\mu$m-diameter droplets. The 2.4-fold and 3.4-fold increase in target mass (compared to the 30 $\mu$m diameter case) increase the number of tin ions that contribute to in-band emission.

In figure 4(b) we show the center-of-mass position $z$ of the target over time and in figure 4(c) the amount of liquid mass associated with a density $\rho > \rho_{\text{vap}}$ remaining in the target over time, which we denote by $m_{\text{liq}}$. Naturally, these curves end at $t = t_{\text{vap}}$. While laser-induced droplet propulsion is a complex process, we investigate the observed displacement of the droplet through a simple one-dimensional model akin to rocket propulsion: one starts off with a droplet of tin of mass $M$, at rest at the origin. The laser ablates the target at a constant rate of $\bar{\mu}$ mg ns$^{-1}$, with all the ablated material flying off in the negative $\hat{z}$-direction at a laser intensity-dependent rate of $\nu(I_{\text{laser}}, t)$ mm ns$^{-1}$ with respect to the droplet. Imposing momentum and energy conservation, we find the following relation for droplet position (see the appendix for the derivation):

$$z(t) = \nu\left(\frac{M-\bar{\mu}t}{\bar{\mu}}\ln\left(\frac{M-\bar{\mu}t}{M}\right)+t\right). \tag{2}$$

It is our task to determine $\bar{\mu}$ and $\nu$. First consider the mass loss rate $\bar{\mu}$. From figure 4(c), we see that the mass loss rate $-\mathrm{d}m_{\text{liq}}/\mathrm{d}t$ is nearly constant up to $t_{\text{vap}}/2$. As such, we can obtain an *empirical* mass loss rate $\mu$ by obtaining the (negative) slope of the line from a linear least-squares fit for $m_{\text{liq}}(t)$ from 0 up to $t_{\text{vap}}/2$. Values for $\mu$ for all laser intensity cases are shown by the blue dots in figure 5. Since trivially $\mu$ should tend to 0 for vanishing intensity, a power law appears appropriate to describe its intensity dependence:

$$\mu = AI_{\text{laser}}^{B}, \tag{3}$$

for some $A$ and $B$, and with $\mu$ in mg ns$^{-1}$ and $I_{\text{laser}}$ in W cm$^{-2}$. A least-squares fit of the data points yields $A = 8.44\times10^{-12}$ and $B = 0.45$ in units consistent with $\mu$ and $I_{\text{laser}}$, and the result is shown in figure 5 as the blue dashed curve. Previous studies of tin mass ablation rate also reveal a power-law dependence on intensity; see for example the experimental work of Burdt *et al* [62] who, by irradiating planar tin targets with short laser pulses (6.5 ns full width at half maximum) and inferring the crater depth, report an exponent of 0.56, in agreement with the theoretical work of Dahmani and Kerdja [63]. Furthermore, a smaller exponent of 0.29 is predicted in the theoretical study of Basko *et al* [41]. The value we obtain during the initial phases of droplet evaporation is thus intermediate between these two.

The vaporization time in this model, $t_{\text{vap}}$, is defined as the time at which a mass of $\rho_{\text{vap}}V$ remains:

$$t_{\text{vap}}^{*} = (1-\rho_{\text{vap}}/\rho)\frac{M}{\bar{\mu}} \approx 0.86\frac{M}{\bar{\mu}}. \tag{4}$$

Using the values for $\mu$ obtained from equation (3), one obtains the vaporization time $t_{\text{vap}}^{*}$ represented by the dashed green line in figure 5. This line deviates from the simulated values, represented by the green circles in figure 5, by a proportionality factor (as the notational difference between $\mu$ and $\bar{\mu}$ suggests). This deviation arises because $-\mathrm{d}m_{\text{liq}}/\mathrm{d}t$ abandons constancy

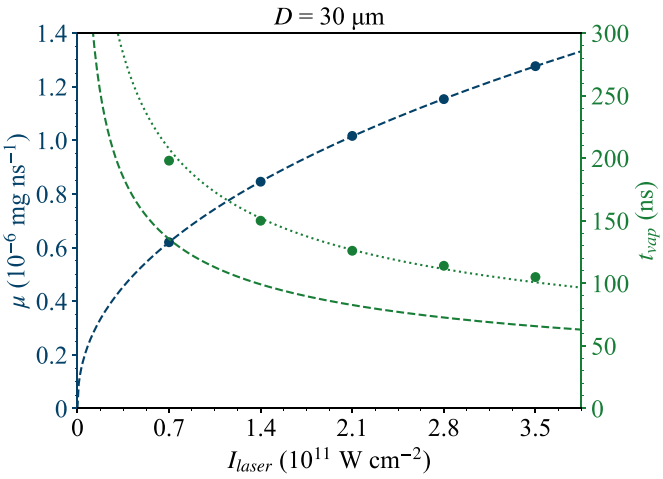


**Figure 5.** The relation between 'initial' mass loss rate $\mu$ (blue) and vaporization time (green) with laser intensity. The blue dots correspond to the mass loss rate $\mu$ (measured from $t = 0$ to $t_{\text{vap}}/2$, see main text) as a function of laser intensity, and the dashed line is equation (3). The green dashed line is the uncorrected vaporization time $t_{\text{vap}}^{*}$ obtained from equation (4). By including the correction factor $c = \mu/\bar{\mu} = 1.53$, one finds good agreement between the simulated values for $t_{\text{vap}}$ (green dots) and the derived intensity-dependent law for $t_{\text{vap}}$, equation (5) (dotted line).

and diminishes from $t_{\text{vap}}/2$ onwards. Using the above values for $\mu$ in the model will therefore under-predict $t_{\text{vap}}$. The correct value for $t_{\text{vap}}$ is obtained by using the mean mass loss rate $\bar{\mu}$, defined as $0.86M/t_{\text{vap}}$, instead. We find that the mean mass loss rate $\bar{\mu}$ and the 'initial' mass loss rate $\mu$ are related by the factor $c = \mu/\bar{\mu}$. With this, the vaporization time can be estimated from the mass loss rate:

$$t_{\text{vap}} = 0.86\frac{M}{\bar{\mu}} = 0.86c\frac{M}{AI^{B}}. \tag{5}$$

Taking the average of $c$ over the five data points, we find that $c = 1.53$. This approach has errors no greater than 5% in estimating $t_{\text{vap}}$; for the specific case of $I = 1.4\times10^{11}$ W cm$^{-2}$, the error is less than 2%. The green dotted line in figure 5 represents equation (5).

Having found values for $\bar{\mu}$ as a function of laser intensity, we next determine the ablation velocity $\nu$. Equation (15) in the appendix suggests that $\nu$ is a power law in $I_{\text{laser}}$ (since $\bar{\mu}$ is also a power law of $I_{\text{laser}}$). This implies $\nu \propto I^{(1-B)/2} \approx I^{0.28}$, a rather weak dependence on $I_{\text{laser}}$. However, this does not provide an adequate prediction of the vaporization position $z_{\text{vap}}$: the simulated value does not follow a power law in $I_{\text{laser}}$ as would be predicted by equation (2) and the above-theorized behavior of $\nu$. In fact, from figure 4(b), one sees that the simulated $z_{\text{vap}}$ values initially decrease with increasing $I_{\text{laser}}$ until $I_{\text{laser}} = 2.1\times10^{11}$ W cm$^{-2}$, beyond which $z_{\text{vap}}$ increases. Whatever the trend in $z_{\text{vap}}$ with increasing laser intensity, its values are highly sensitive to variations in $t_{\text{vap}}$ due to the droplet's high velocity near vaporization.

To circumvent these difficulties, we determine $\nu$ in the following way: We first substitute the expression for $t_{\text{vap}}$ into

equation (2) to derive the position $z_{\text{vap}}$ at which $t_{\text{vap}}$ occurs:

$$z_{\text{vap}} \equiv z\left(t_{\text{vap}}\right) = \frac{M\nu}{\bar{\mu}}\left[\frac{\rho_{\text{vap}}}{\rho}\ln\left(\frac{\rho_{\text{vap}}}{\rho}\right) + \left(1 - \frac{\rho_{\text{vap}}}{\rho}\right)\right] \quad (6)$$

$$\approx 0.58\frac{M\nu}{\bar{\mu}}. \quad (7)$$

Second, using values of $z_{\text{vap}}$ predicted by the simulations, we solve equation (7) for $\nu$. We now have everything necessary to plot equation (2), which is shown by the red dashed lines in figure 4(b) for the various laser intensity cases. For $I_{\text{laser}} < 1.4 \times 10^{11}$ W cm$^{-2}$, the model under-predicts $t_{\text{vap}}$, and for $I_{\text{laser}} > 1.4 \times 10^{11}$ W cm$^{-2}$ it over-predicts $t_{\text{vap}}$; this arises from deviations between simulated $t_{\text{vap}}$ values (green data points in figure 5) and the analytic $t_{\text{vap}}$ (green dashed line in figure 5). These things notwithstanding, our relatively simple one-dimensional model is adept at qualitatively explaining the shape of the trajectory curve.

Simulation results for the irradiation of $D = 45\,\mu$m diameter droplets are shown in figures 8–10 in the appendix. The shapes are qualitatively similar to that of the $D = 30\,\mu$m case, although $z_{\text{vap}}$ and $t_{\text{vap}}$ are substantially larger than the $D = 30\,\mu$m case given the $1.5^3$-fold increase in mass of the target. The power law equation (3) is also found to hold true with nearly the same exponent: $B = 0.46$. The laser and EUV source parameters associated with this droplet diameter, as well as an intermediate value of $D = 40\,\mu$m, are also provided in table 1. Importantly, we see that laser irradiation of $D = 45\,\mu$m droplets with $I_{\text{laser}} \geqslant 1.4 \times 10^{11}$ W cm$^{-2}$ can generate $E_{\text{inband}} > 100$ mJ.

### 3.3. Laser refraction and EUV source properties

In the simulations presented thus far, only laser absorption and reflection in the plasma were modelled; the effects of laser refraction were ignored. As discussed in [57], refraction of the laser beam in underdense plasma regions can induce unstable plasma outflows. This can result in the focusing of laser light into regions with a depression in the electron density; this is called hydrodynamic self-focusing instability. Localized regions of high temperatures emerge ('hot spots'—see figure 6 of [43]), which, alongside the plasma outflow, fluctuate significantly in both space and time. We now investigate the effect of including laser refraction in our model on EUV source properties.

In figure 6, we compare the instantaneous CE values for two cases: one that does not consider laser refraction in the plasma ('no refraction'—red curve, seen previously in figure 4) and one that models laser refraction in the plasma ('refraction'—blue curve). The two cases are initially similar in CE, where the 'refraction' case is seen to oscillate about the 'no refraction' CE value. However, around 75 ns, the CE in the 'refraction' case suddenly drops by approximately 20% before stabilizing; at 125 ns, the CE starts dropping to zero, and the droplet vaporizes at 136 ns. All in all, 23.2 mJ of in-band radiation is emitted in the $2\pi$ sr solid angle of the collector mirror, approximately 82% of the 'no refraction' case.

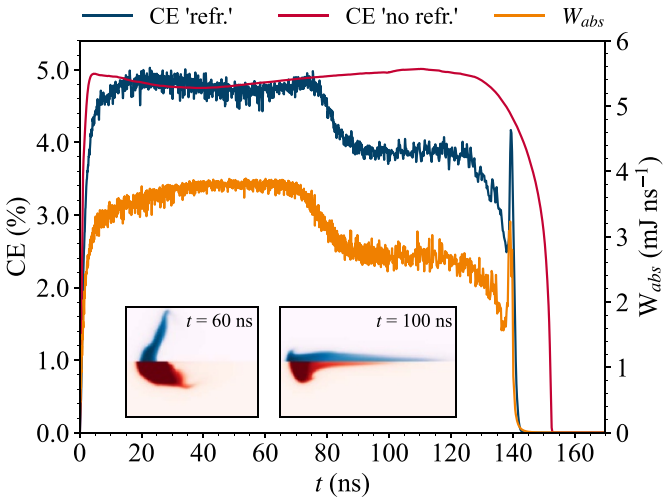


**Figure 6.** A comparison of time-resolved CE of simulations for the 'refraction' case (blue curve) and the 'no refraction' case (red curve). Both cases represent laser irradiation of a 30 $\mu$m diameter droplet with $I_{\text{laser}} = 1.4 \times 10^{11}$ W cm$^{-2}$. Absorbed laser energy in the 'refraction' case is shown by the orange curve. The two insets show the density distributions at 60 ns (total image size $60 \times 50\,\mu$m) and 100 ns ($80 \times 50\,\mu$m). The 'refraction' case is shown in the upper half, the 'no refraction' case in the lower. Note that the upper and lower halves of the insets are aligned for comparison and do not actually match in $z$ position.

To understand the drop in CE in the 'refraction' case, we present in figure 6 two insets showing the density profiles of the targets before and after the drop in CE, at 60 and 100 ns respectively. The upper half shows the 'refraction' case (blue) and the bottom half shows the 'no refraction' case (red). Within this interval, the target in the 'refraction' case changes shape from flat to elongated along the $z$-axis; this reduces its cross section, and consequently, a fraction of the laser light will fail to be absorbed. This is evident from the absorbed laser power curve shown in orange in figure 6, which closely follows the shape of the CE curve including the drop at 75 ns and the spike at 139 ns. Despite the simulation's inherent stochasticity, the oscillatory trend and subsequent drop in CE are reproduced for repeated simulations using identical laser and target parameters. Therefore, we attribute the discrepancy in CE (between the 'refraction' and 'no-refraction' cases) to the morphological difference of the droplet target between the two cases, and draw attention to the importance of droplet morphology for long-pulse irradiation schemes.

## 4. Conclusion

In this paper, we have elucidated various aspects of long-pulse, 2 $\mu$m-wavelength laser irradiation of tin droplets in the context of EUV sources for nanolithography. The main point is that the usage of large droplets and long pulses is, in theory, able to produce tens of millijoules of in-band radiation. While a laser intensity of $0.7 \times 10^{11}$ W cm$^{-2}$ has previously been identified as CE-optimal, we find that even greater amounts of in-band-energy-per-shot can be produced by increasing the intensity at minimal loss in CE. Moreover, we have quantified the EUV

source size and have shown that ∼74% of the in-band energy is emitted within half the total propulsion distance regardless of droplet size or laser intensity.

We presented a simple one-dimensional model to predict the droplet trajectory and vaporization time. By calculating the ablation rate and deriving a scaling law, this model gives accurate and consistent estimations of the vaporization time for the range of laser intensities considered. These findings, coupled with those mentioned above, provide impetus for further development of EUV sources based on single-pulse, 2 $\mu$m-wavelength irradiation of tin droplets.

## Data availability statement

All data that support the findings of this study are included within the article (and any supplementary files).

## Acknowledgments

We would like to thank Wim van der Zande, Jorge Gonzalez, Elio Champenois, Haining Wang, Adam Higginson and Michael Purvis for useful discussions. This work has been carried out at the Advanced Research Center for Nanolithography (ARCNL). ARCNL is public–private partnership with founding partners UvA, VU, NWO-I and ASML, and associate partner RUG. This work made use of the Dutch national e-infrastructure with the support of the SURF Cooperative using Grant Nos. EINF-3119 and EINF-6930.

## Appendix

### *A.1. Simulation results for 45 $\mu$m diameter droplet*

The following four plots, figures 7–10, are identical to figures 2–5 in the main text but correspond to laser irradiation of a $D = 45\,\mu$m-diameter droplet. The trends shown in these plots are qualitatively very similar to the $D = 30\,\mu$m case, albeit that the values for $E_{\mathrm{inband}}$ and $z_{\mathrm{vap}}$ and $t_{\mathrm{vap}}$ are significantly higher here given the increased target mass.

### *A.2. Derivation of the droplet propulsion model*

In the following, we derive a simple model, akin to rocket propulsion, to predict the droplet trajectory dynamics. Consider a droplet of tin of mass $M$ initially at rest at the origin. The laser ablates the target at a constant rate of $\bar{\mu}$ mg ns$^{-1}$, and all the ablated material moves in the negative $\hat{z}$-direction at a laser intensity and (*a priori*) time-dependent rate of $\nu(I,t)$ mm ns$^{-1}$ with respect to the droplet. For initial conditions we assume $z(0) = 0$, $V(0) \equiv \dot{z}(0) = 0$. Finally, we require that momentum and energy be conserved. We therefore have two functions with two unknowns. Conservation of momentum (droplet momentum plus the momentum of the debris ablated at every interval in time) can be written as

$$(M - \bar{\mu}t)\,V(t) = \int_0^t \bar{\mu}\,(\nu(I,\tau) - V(\tau))\,\mathrm{d}\tau. \tag{8}$$

Taking the derivative on both sides with respect to $t$,

$$-\bar{\mu}V(t) + (M - \bar{\mu}t)\,\dot{V}(t) = \bar{\mu}\nu(I,t) - \bar{\mu}V(t), \tag{9}$$

$$(M - \bar{\mu}t)\,\dot{V}(t) = \bar{\mu}\nu(I,t). \tag{10}$$

Conservation of energy is implemented by positing that the total kinetic energy in the system increases due to the energy supply by the laser:

$$\frac{1}{2}\bar{\mu}\,(\nu(I,t) - V(t))^2 + \frac{\mathrm{d}E_{\mathrm{k,droplet}}}{\mathrm{d}t} = \eta_{\mathrm{k}}\sigma I, \tag{11}$$

where $\eta_{\mathrm{k}}$ is the fraction of laser power that is converted into kinetic energy (which is taken as constant) and $\sigma$ is the cross-section of the (fully absorbed) laser beam. It is assumed that all laser light is absorbed (thus with no light escaping, the laser power is proportional to the intensity). The droplet's kinetic energy is given by

$$E_{\mathrm{k,droplet}} = \frac{1}{2}\,(M - \bar{\mu}t)\,V(t)^2. \tag{12}$$

Substituting this into equation (11) and reordering terms we obtain:

$$\frac{1}{2}\bar{\mu}\nu(I,t)^2 - \bar{\mu}\nu(I,t)\,V(t) + (M - \bar{\mu}t)\,V(t)\,\dot{V}(t) = \eta_{\mathrm{k}}\sigma I. \tag{13}$$

From equation (10) we find that the second and third terms cancel:

$$\frac{1}{2}\bar{\mu}\nu(I,t)^2 = \eta_{\mathrm{k}}\sigma I. \tag{14}$$

And thus we find our expression for $\nu$:

$$\nu(I,t) = \sqrt{2\sigma\eta_{\mathrm{k}}I/\bar{\mu}}. \tag{15}$$

Note that this function is constant in time: $\nu(I,t) = \nu(I)$. To derive $V(t)$, we go back to equation (10):

$$\dot{V}(t) = \frac{\bar{\mu}\nu}{M - \bar{\mu}t}. \tag{16}$$

Since $\nu$ is constant, this integral is straightforward:

$$V(t) = \int_0^t \frac{\bar{\mu}\nu}{M - \bar{\mu}\tau}\mathrm{d}\tau = \nu\ln\left(\frac{M}{M - \bar{\mu}t}\right). \tag{17}$$

Finally, the droplet position $z(t)$ is computed by integrating again:

$$z(t) = \int_0^t V(\tau)\,\mathrm{d}\tau = \nu\left(\frac{M - \bar{\mu}t}{\bar{\mu}}\ln\left(\frac{M - \bar{\mu}t}{M}\right) + t\right). \tag{18}$$

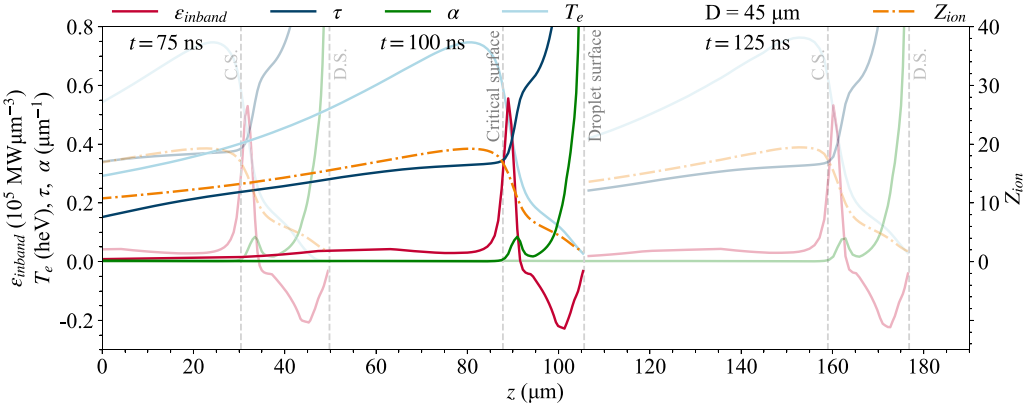


**Figure 7.** Same as figure 2 for a $D = 45\,\mu$m-diameter droplet.

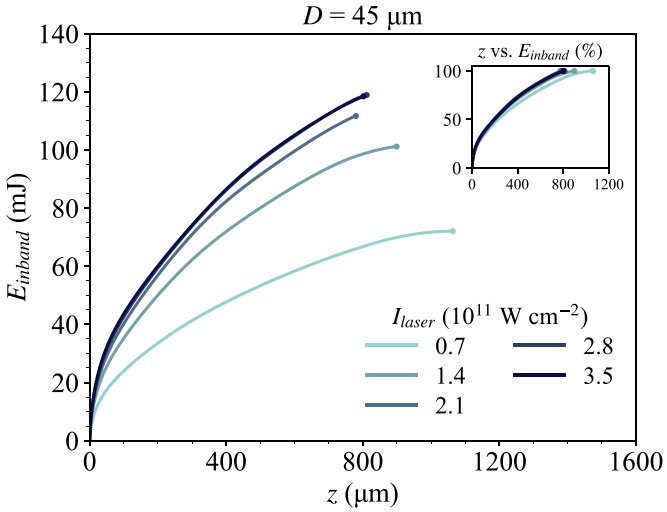


**Figure 8.** Same as figure 3 for a $D = 45\,\mu$m-diameter droplet.

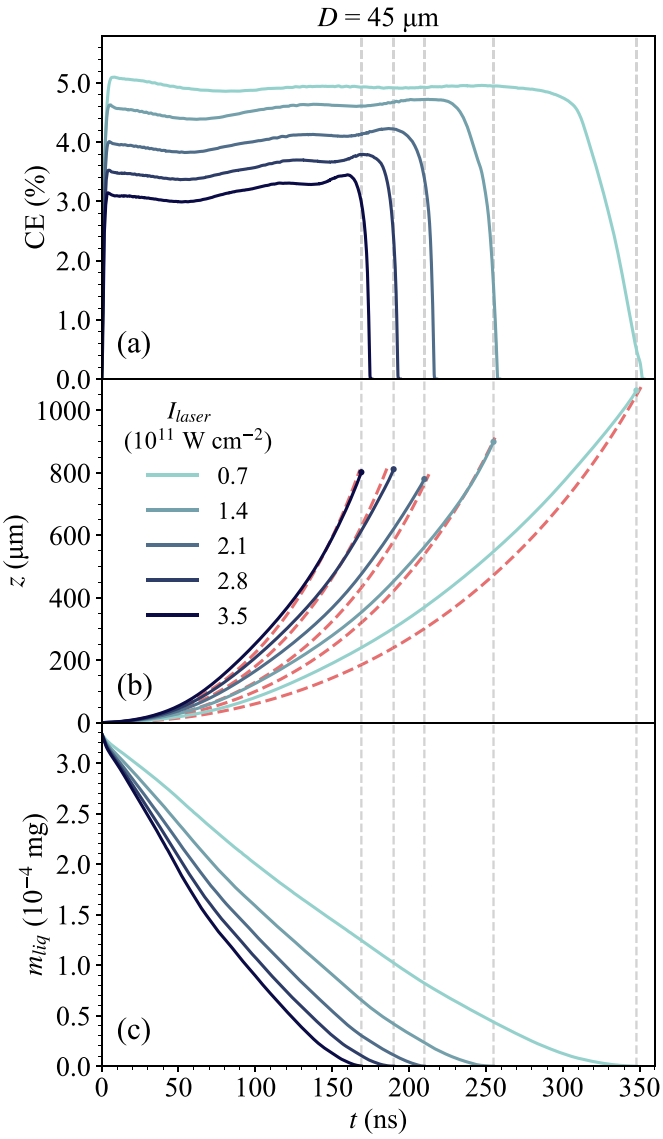


**Figure 9.** Same as figure 4 for a $D = 45\,\mu$m-diameter droplet.

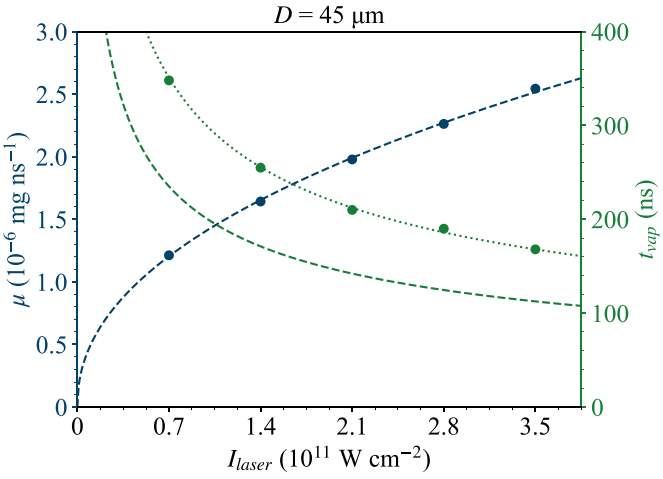


**Figure 10.** Same as figure 5 for a $D = 45\,\mu$m-diameter droplet. The blue dashed line, equation (3), has parameter values $A = 1.31 \times 10^{-11}$ and $B = 0.46$, and the dashed green line, equation (5), uses $c = 1.49$.

## ORCID iDs

S J J de Lange https://orcid.org/0000-0002-9941-6019
D J Hemminga https://orcid.org/0000-0002-4038-3646
Y Mostafa https://orcid.org/0000-0002-4418-680X
R A Meijer https://orcid.org/0000-0003-1738-4488
O O Versolato https://orcid.org/0000-0003-3852-5227
J Sheil https://orcid.org/0000-0003-3393-9658

## References

[1] Bleiner D, Costello J, Dortan F, O'Sullivan G, Pina L and Michette A (eds) 2014 *Short Wavelength Laboratory Sources: Principles and Practices* (The Royal Society of Chemistry)
[2] O'Sullivan G D and Faulkner R 1994 Tunable narrowband soft x-ray source for projection lithography *Opt. Eng.* **33** 3978–83
[3] Burkhalter P G, Feldman U and Cowan R D 1974 Transitions in highly ionized Sn spectra from a laser-produced plasma *J. Opt. Soc. Am.* **64** 1058–62
[4] Harilal S S, Phillips M C, Froula D H, Anoop K K, Issac R C and Beg F N 2022 Optical diagnostics of laser-produced plasmas *Rev. Mod. Phys.* **94** 035002
[5] Legall H *et al* 2012 Compact x-ray microscope for the water window based on a high brightness laser plasma source *Opt. Express* **20** 18362–9
[6] Fahy K *et al* 2021 Compact cell imaging device (CoCID) provides insights into the cellular origins of viral infections *J. Phys. Photon.* **3** 031002
[7] Zylstra A B *et al* 2022 Burning plasma achieved in inertial fusion *Nature* **601** 542–8
[8] Moore S K 2018 EUV lithography finally ready for fabs *IEEE Spectr.* **55** 46–48
[9] Bakshi V (ed) 2018 *EUV Lithography* 2nd edn (SPIE Press)
[10] Versolato O O 2019 Physics of laser-driven tin plasma sources of EUV radiation for nanolithography *Plasma Sources Sci. Technol.* **28** 083001
[11] Tomita K *et al* 2017 Time-resolved two-dimensional profiles of electron density and temperature of laser-produced tin plasmas for extreme-ultraviolet lithography light sources *Sci. Rep.* **7** 12328
[12] Torretti F, Liu F, Bayraktar M, Scheers J, Bouza Z, Ubachs W, Hoekstra R and Versolato O 2019 Spectral characterization of an industrial EUV light source for nanolithography *J. Phys. D: Appl. Phys.* **53** 055204
[13] Sheil J, Versolato O, Bakshi V and Scott H 2023 Review of the 1st EUV light sources code comparison workshop *Atoms* **11** 130
[14] Svendsen W and O'Sullivan G 1994 Statistics and characteristics of xuv transition arrays from laser-produced plasmas of the elements tin through iodine *Phys. Rev.* A **50** 3710–8
[15] Sasaki A, Sunahara A, Furukawa H, Nishihara K, Fujioka S, Nishikawa T, Koike F, Ohashi H and Tanuma H 2010 Modeling of radiative properties of Sn plasmas for extreme-ultraviolet source *J. Appl. Phys.* **107** 113303
[16] O'Sullivan G *et al* 2015 Spectroscopy of highly charged ions and its relevance to EUV and soft x-ray source development *J. Phys. B: At. Mol. Opt. Phys.* **48** 144025
[17] Torretti F *et al* 2020 Prominent radiative contributions from multiply-excited states in laser-produced tin plasma for nanolithography *Nat. Commun.* **11** 2334
[18] Bajt S, Alameda J B, Barbee T W Jr, Clift W M, Folta J A, Kaufmann B and Spiller E A 2002 Improved reflectance and stability of Mo-Si multilayers *Opt. Eng.* **41** 1797–804
[19] Nishihara K *et al* 2008 Plasma physics and radiation hydrodynamics in developing an extreme ultraviolet light source for lithography *Phys. Plasmas* **15** 056708
[20] Fomenkov I *et al* 2017 Light sources for high-volume manufacturing EUV lithography: technology, performance and power scaling *Adv. Opt. Technol.* **6** 173–86
[21] Schupp R *et al* 2019 Efficient generation of extreme ultraviolet light from Nd:YAG-driven microdroplet-tin plasma *Phys. Rev. Appl.* **12** 014010
[22] Umstadter K, Graham M, Purvis M, Schafgans A, Stewart J, Mayer P and Brown D 2023 EUV light source for high-NA and low-NA lithography *Proc. SPIE* **12494** 124940Z
[23] Siders C W, Bayramian A J, Erlandson A C, Galvin T C, Langer S, Sistrunk E F and Spinka T M 2018 New architectures for PW-scale high peak power lasers scalable to near-MW average powers and their application to EUV generation *Source Workshop* (*S22*) (EUV Litho Inc.)
[24] Tamer I, Reagan B A, Galvin T, Galbraith J, Sistrunk E, Church A, Huete G, Neurath H and Spinka T 2021 Demonstration of a compact, multi-joule, diode-pumped Tm:YLF laser *Opt. Lett.* **46** 5096–9
[25] Langer S, Siders C, Galvin T, Scott H and Sistrunk E 2019 Simulations of EUV sources driven by $CO_2$ and thulium lasers *Source Workshop* (*S94*) (EUV Litho Inc.)
[26] Reagan B *et al* 2022 1 GW peak power and 100 J pulsed operation of a diode-pumped $\lambda = 1.9$ $\mu$m laser *Source Workshop* (*S22*) (Advanced Photon Technologies, NIF and Photon Science, Lawrence Livermore National Laboratory, DOE/NNSA (EUV Litho Inc.))
[27] Tamer I *et al* 2022 1 GW peak power and 100 J pulsed operation of a diode-pumped Tm:YLF laser *Opt. Express* **30** 46336–43
[28] Behnke L *et al* 2021 Extreme ultraviolet light from a tin plasma driven by a 2-$\mu$m-wavelength laser *Opt. Express* **29** 4475–87
[29] Schupp R, Behnke L, Sheil J, Bouza Z, Bayraktar M, Ubachs W, Hoekstra R and Versolato O O 2021 Characterization of 1- and 2-$\mu$m-wavelength laser-produced microdroplet-tin plasma for generating extreme-ultraviolet light *Phys. Rev. Res.* **3** 013294
[30] Schupp R *et al* 2021 Characterization of angularly resolved EUV emission from 2-$\mu$m-wavelength laser-driven Sn plasmas using preformed liquid disk targets *J. Phys. D: Appl. Phys.* **54** 365103
[31] Mostafa Y, Behnke L, Engels D J, Bouza Z, Sheil J, Ubachs W and Versolato O O 2023 Production of 13.5 nm light with 5% conversion efficiency from 2 $\mu$m laser-driven tin microdroplet plasma *Appl. Phys. Lett.* **123** 234101
[32] Behnke L, Salumbides E J, Göritz G, Mostafa Y, Engels D, Ubachs W and Versolato O 2023 High-energy parametric oscillator and amplifier pulsed light source at 2-$\mu$m *Opt. Express* **31** 24142–56
[33] Hemminga D J, Versolato O O and Sheil J 2023 Simulations of plasmas driven by laser wavelengths in the 1.064–10.6 $\mu$m range for their characterization as future extreme ultraviolet light sources *Phys. Plasmas* **30** 033301
[34] Sizyuk T and Hassanein A 2020 Tuning laser wavelength and pulse duration to improve the conversion efficiency and performance of EUV sources for nanolithography *Phys. Plasmas* **27** 103507
[35] Yuan Y, Ma Y Y, Wang W P, Chen S J, Cui Y, Zi M, Yang X H, Zhang G B and Leng Y X 2021 Enhancing the conversion efficiency of extreme ultraviolet light sources using a 2 $\mu$m wavelength laser *Plasma Phys. Control. Fusion* **64** 025001
[36] Shi Z Y, Yuan Y, Wang W P, Ma Y Y, Sun X Y, Lin N and Leng Y X 2023 Enhanced extreme ultraviolet conversion efficiency of a 2 $\mu$m laser-driven preformed tin-droplet target using short picosecond pre-pulses *Phys. Plasmas* **30** 043107

[37] Basko M, Maruhn J and Tauschwitz A 2010 Development of a 2D radiation-hydrodynamics code RALEF for laser plasma simulations *GSI Rep.* **1** 410
[38] Basko M M, Sasorov P V, Murakami M, Novikov V G and Grushin A S 2012 One-dimensional study of the radiation-dominated implosion of a cylindrical tungsten plasma column *Plasma Phys. Control. Fusion* **54** 055003
[39] Tauschwitz A, Basko M, Frank A, Novikov V, Grushin A, Blazevic A, Roth M and Maruhn J 2013 2D radiation-hydrodynamics modeling of laser-plasma targets for ion stopping measurements *High Energy Density Phys.* **9** 158–66
[40] Malko S *et al* 2022 Proton stopping measurements at low velocity in warm dense carbon *Nat. Commun.* **13** 2893
[41] Basko M M, Novikov V G and Grushin A S 2015 On the structure of quasi-stationary laser ablation fronts in strongly radiating plasmas *Phys. Plasmas* **22** 053111
[42] Basko M 2016 On the maximum conversion efficiency into the 13.5-nm extreme ultraviolet emission under a steady-state laser ablation of tin microspheres *Phys. Plasmas* **23** 083114
[43] Kurilovich D, Basko M M, Kim D A, Torretti F, Schupp R, Visschers J C, Scheers J, Hoekstra R, Ubachs W and Versolato O O 2018 Power-law scaling of plasma pressure on laser-ablated tin microdroplets *Phys. Plasmas* **25** 012709
[44] Basko M, Maruhn J and Tauschwitz A 2017 RALEF-2D: A 2D hydrodynamic code with heat conduction and radiation transport *RALEF 2D Main Report* (available at: www.basko.net/mm/RALEF/ralef-main-report.pdf)
[45] Addessio F L, Baumgardner J R, Dukowicz J K, Johnson N L, Kashiwa B A, Rauenzahn R M and Zemach C 1992 CAVEAT: a computer code for fluid dynamics problems with large distortion and internal slip *Report* No. LA-10613-MS-Rev. 1, UC-32 (Los Alamos National Laboratory)
[46] Livne E and Glasner A 1985 A finite difference scheme for the heat conduction equation *J. Comput. Phys.* **58** 59–66
[47] Basko M M, Maruhn J and Tauschwitz A 2009 An efficient cell-centered diffusion scheme for quadrilateral grids *J. Comput. Phys.* **228** 2175–93
[48] Dedner A and Vollmöller P 2002 An adaptive higher order method for solving the radiation transport equation on unstructured grids *J. Comput. Phys.* **178** 263–89
[49] Nikiforov A F, Novikov V G and Uvarov V B 2005 *Quantum-Statistical Models of Hot Dense Matter: Methods for Computation Opacity and equation of State (Progress in Mathematical Physics)* (Birkhauser)
[50] Vichev I, Solomyannaya A, Grushin A and Kim D 2019 On certain aspects of the THERMOS toolkit for modeling experiments *High Energy Density Phys.* **33** 100713
[51] Scott H A, Harte J A, Foord M E and Woods D T 2022 Using tabulated NLTE data for Hohlraum simulations *Phys. Plasmas* **29** 082703
[52] Castor J I 2004 *Radiation Hydrodynamics* (Cambridge University Press)
[53] Elezier S 2002 *The Interaction of High-Power Lasers With Plasmas* (CRC Press)
[54] Faik S, Tauschwitz A and Iosilevskiy I 2018 The equation of state package FEOS for high energy density matter *Comput. Phys. Commun.* **227** 117–25
[55] More R M, Warren K H, Young D A and Zimmerman G B 1988 A new quotidian equation of state (QEOS) for hot dense matter *Phys. Fluids* **31** 3059–78
[56] Hernandez-Rueda J, Liu B, Hemminga D J, Mostafa Y, Meijer R A, Kurilovich D, Basko M, Gelderblom H, Sheil J and Versolato O O 2022 Early-time hydrodynamic response of a tin droplet driven by laser-produced plasma *Phys. Rev. Res.* **4** 013142
[57] Basko M M and Tsygvintsev I P 2017 A hybrid model of laser energy deposition for multi-dimensional simulations of plasmas and metals *Comput. Phys. Commun.* **214** 59–70
[58] Poirier L, Hemminga D J, Lassise A, Assink L, Hoekstra R, Sheil J and Versolato O O 2022 Strongly anisotropic ion emission in the expansion of Nd:YAG-laser-produced plasma *Phys. Plasmas* **29** 123102
[59] Hickstein D D, Gibson S T, Yurchak R, Das D D and Ryazanov M 2019 A direct comparison of high-speed methods for the numerical Abel transform *Rev. Sci. Instrum.* **90** 065115
[60] Salzmann D 1998 *Atomic Physics in Hot Plasmas* (Oxford University Press)
[61] Fujioka S *et al* 2004 Suppression of the Rayleigh–Taylor instability due to self-radiation in a multiablation target *Phys. Rev. Lett.* **92** 195001
[62] Burdt R A, Yuspeh S, Sequoia K L, Tao Y, Tillack M S and Najmabadi F 2009 Experimental scaling law for mass ablation rate from a Sn plasma generated by a 1064 nm laser *J. Appl. Phys.* **106** 033310
[63] Dahmani F and Kerdja T 1991 Planar laser-driven ablation model for nonlocalized absorption *Phys. Fluids* B **3** 1232–40